Multishot Tomography for High-Resolution In Situ Subtomogram Averaging.

S. Khavnekar[1*], W. Wan[3], P. Majumder[1], W. Wietrzynski, P. S. Erdmann[1,2#]and J. M. Plitzko[1#]

[1] MPI for Biochemistry

[2] Human Technopole

[3] Vanderbilt University

* 1st Author

corresponding authors

Correspondence should be addressed to:

Philipp S Erdmann philipp.erdmann@fht.org

Jürgen M Plitzko plitzko@biochem.mpg.de

Abstract

Cryo-electron tomography (cryo-ET) and subtomogram averaging (STA) can resolve protein complexes at near atomic resolution, and when combined with focused ion beam (FIB) milling, macromolecules can be observed within their native context. Unlike single particle acquisition (SPA), cryo-ET can be slow, which may reduce overall project throughput. We here propose a fast, multi-position tomographic acquisition scheme based on beam-tilt corrected beam-shift imaging along the tilt axis, which yields sub-nanometer in situ STA averages.

Main

Since the resolution revolution[1], cryo-electron microscopy has yielded numerous structures of biomolecular complexes at near-atomic resolution. Two key factors have made this advance possible: development of new imaging hardware, first and foremost direct electron detectors (DEDs)[2], and automation of both acquisition and processing[3–6]. For both SPA and STA, each individual particle has a low signal to noise ratio (SNR), and hence imaging large numbers of the same molecular species, followed by alignment, averaging, and reconstruction is necessary in order to reveal their high-resolution details. SPA has become the main method for high resolution structure determination by cryo-EM. It relies on 2D projections of discreet particles, and ideal specimens contain a monolayer of particles to minimize ice thickness and prevent overlapping projections. STA first requires reconstruction of a tomogram, a 3D representation of the specimen. From there, molecules are identified and averaged in 3D, removing issues related to overlapping particles. Despite its generally accepted versatility, there are inherent limitations to SPA and

its derivatives, since they require purification and concentration of the target of interest. Accordingly, all information on the molecular sociology of the cellular components is lost. Moreover, single particle cryo-EM is sensitive to concentration and overlap of particles. Tomography and subtomogram averaging on the other hand use three-dimensional data, and consequently are well equipped to handle both. When combined with suitable preparation techniques, e.g. FIB milling, in situ STA can be used to interrogate the native architecture of cellular structures without the need for purification, highlighted recently by several sub-nanometer in situ structures.[7–9]

For both STA and SPA, particle numbers and therefore acquisition speed are determining factors for sorting out molecular heterogeneity and achieving high resolution. Symmetrical, repetitive, and/or abundant structures are therefore particularly well suited for high resolution studies. Since the introduction of fast DEDs, the acquisition time is no longer limited by the cameras, and modern single tilt stages offer improved stability compared to dual axis holders.[10] However, stage movement and the resulting settling times still take a major toll on the overall acquisition time[11]. This is especially true for tomography, where the sample needs to be tilted over a broad range of angles (usually ± 60º), while individual projection images are recorded. This requires that the sample be kept in eucentric height and on the same field of view as accurately as possible. While modern dose-symmetric tilt schemes help to distribute the available electron dose as efficiently as possible,[11] as opposed to monodirectional or bidirectional schemes they are more time consuming. To address this problem, fast tilting schemes have been developed that rely on pre-calibrated stage movements rather than tracking and focusing on each individual tilt.[10,12] However, the data quality from these fast tomograms may require additional tilt-series refinement approaches. [13–15]

While not as essential, stage stability still is a factor to consider in SPA and defined settling times are used to allow stage drift to stabilize after each stage move. To work around this limitation, beam image-shift (BIS) based acquisition (multishot) has been developed (Fig. 1A).[16] Using this technique, several positions within the same hole of a grid and even adjacent holes can be imaged using just image shift (IS) and without additional stage movements. The IS-induced coma can be compensated for within modern acquisition software packages,[17] leaving no or very little beam tilt to be considered during reconstruction.

In cryo-electron tomography, particle numbers are in general more limited than in SPA since tomogram acquisition requires a lot of mechanical movement and therefore is slow compared to single particle acquisition. A lot of the movements could be substituted by BIS, however multishot acquisition has not yet been applied to subtomogram averaging from tomographic reconstructions. With a few limitations (see below) and based on the implementation of constrained single particle tomography (CSPT),[18] the same concept should nonetheless be applicable to cryo-ET in general, but in particular to in situ tomography, where it would significantly increase its throughput. For a perfect (i.e. flat) sample, imaging along the tilt axis does not require any specialize tracking, because points along this axis are co-planar and co-focal.

Consequently, there should be no to very little tilt-induced x,y movement for a sample at eucentric height. Multiple tilted projection images can therefore be taken using BIS-based acquisition if the imaging areas are co-planar. Tilt series can therefore simply be "expanded" and multiple tomograms be recorded at the same time. Such an axial multishot scheme should be straightforward to implement because all required components have already been implemented for SPA. In SerialEM for example, we realized multishot tomography with just a few changes to the existing dose-symmetric acquisition scripts, or by using the built-in tilt-series (TS) controller with some additional scripting (See Methods). Even though slightly more time-consuming, we chose to implement a dose-symmetric routine, as our screening of different tilt series (Supporting Fig. 1) and previous publications suggested that there is a substantial gain in resolution compared to the other options.[19] While off-axis shots can be implemented, they require additional tracking and external software,[20] so we opted to just consider on-axis imaging for now.

Results and Discussion

As a proof of concept, we first tested if x,y shifts were small enough to not lose tracking over an extended axial multishot tilt series. Therefore, we recorded tomograms on carbon with five shots (sequence 0, +2, -2, +1, -1), each time tracking on both the focusing and the center record area (0 shot). The entire series thereby spanned a total of 4 µm along the tilt axis between the +2 and -2 shots. For examples on other possible multishot schemes and nomenclature see Supporting Fig. 2. After tomogram reconstruction, relative shifts of the individual fields of view were calculated with respect to the initial (0) tilt. Results for the most extreme shot (+2 vs. 0) are summarized in Fig. 1C (See Supporting Fig. 3 for all other shots). While the illustrated examples show acquisition on a holey grid, the concept extends to more general sample types such as lacey grids or focused ion beam-milled lamellas (see below) and does not – in general – require grids aligned with the tilt axis.

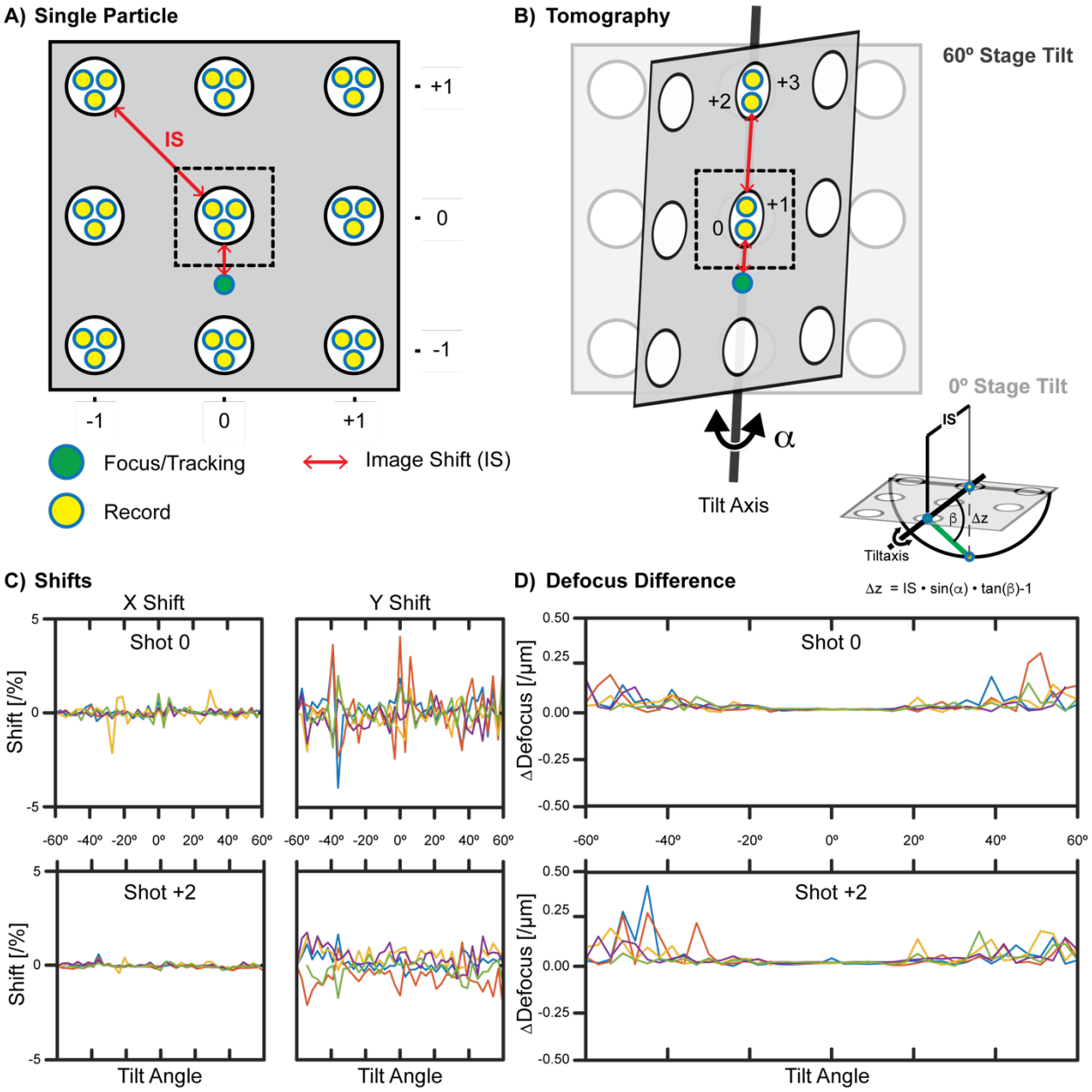

Figure 1. A) The concept of multishot imaging in SPA using beam image shift (BIS) on a holey grid. Positions are indexed from [±n,±m] (for an n-by-m grid). B) Proposed application of BIS to cryo-ET. Here, only +n to -n shifts are acquired along the tilt axis for an "ideally aligned" holey carbon grid. The expected displacement is a function of x-tilt (β), applied image shift (IS) and stage tilt (α). C) Measured x,y shifts of tilt series on carbon, relative to the full image size and as function of tilt angle and shot position for a 5-shot series (sequence: 0,+2,-2,+1,-1). The 0 and +2 shots (2 µm IS) are compared. D) Comparison of defocus difference for the 0 and +2 shots of the same tilt series.

For an ideal specimen with no x-tilt (β), shifts parallel to the tilt-axis are expected to be of similar magnitude with regards to tracking errors after stage tilting. Similarly, difference in defocus, which could also vary as

a function of IS and β (Fig. 1B small insert), would be expected, however were observed to be stable over the multishot tilt series on carbon (Fig. 1D; Supporting Fig. 2).

To evaluate the attainable resolution, we next tested the axial multishot scheme on purified (*in vitro*) non-symmetrical (C1) and symmetrical (D7) particles, i.e. ribosomes from *E. coli* and 20S proteasomes from *T. acidophilum*, on the same grid. After acquiring both single and double shot tilt series, we subjected them to our STA workflow and obtained sub-nanometer resolution averages both in Relion[21] and STOPGAP[22] from just a few thousand particles without the need for tilt series refinement. The D7 symmetrical 20S proteasome (5.2k particles) reached 4.7 Å. Additionally, the 8.3 Å 70S ribosome average (C1) show that this resolution is not simply due to virtual inflation of particle numbers because of high particle symmetry (Fig. 2A & B; Supporting Fig. 3).

To address if there is any variation in image quality with the extent of the BIS, we recorded a series of 5x axial multishots on purified *C. reinhardtii* RuBisCo complexes, which are significantly smaller than both ribosomes and 20S proteasomes. We then divided the data based on their image shifts and hence their relative position in the series. As can be seen from Supporting Fig. 4, no significant difference in resolution was found between the zero (0) and the ±1 and ±2 shots, implying that the residual IS-induced beam tilt after coma-vs-IS alignment is negligible and does not affect subtomogram data quality when performing multishot cryo-ET on *in vitro* samples.

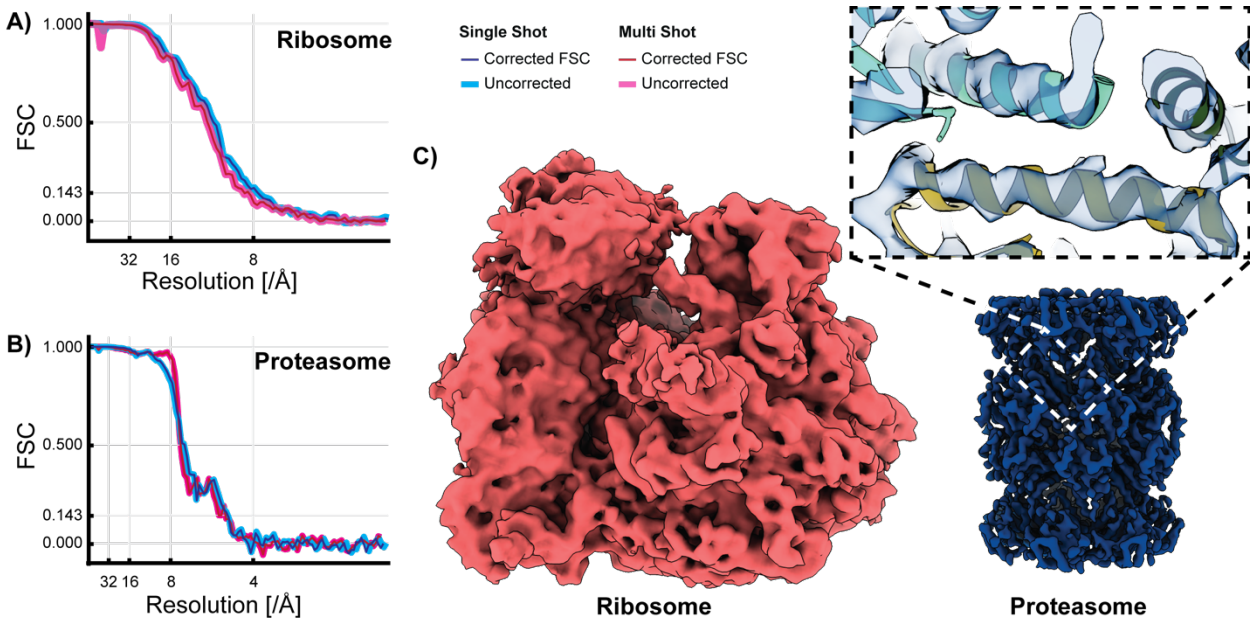

Figure 2. A) Obtainable resolution using two shots on C1 particless (ribosome from E. Coli) at 7.8 Å (single) vs. 8.3 Å (multi) resolution. B) Same for D7 20S proteasome (from T. acidophilum) particles at 4.7 Å (both; FSC = 0.143). C) Subtomogram averages of both species (from Relion) in the multishot acquisition with zoom in on a helix of the T20S proteasome.

No significant tilt-based offset along the tilt axis is expected for sufficiently flat samples. Multishot tomography along the tilt axis of *in vitro* samples is therefore only limited by the hole size vs. beam diameter and grid orientation relative to the tilt axis. For large holes such as multi-A, beam-induced motion may pose a problem, but can be reduced using a thin, continuous support film (e.g. graphene oxide or carbon) as is commonplace for SPA. For in situ samples on the other hand, FIB-milling results in a pre-tilt of the lamella with respect to the surface of the grid support. This pre-tilt is perpendicular to the milling axis. When loading lamella grids, they are rarely perfectly aligned (perpendicular) with the TEM's stage, resulting in a significant x-tilt of up to 5-11 degrees. To investigate, how well the axial multishot scheme would perform on cryo-FIB milled lamellas, we prepared samples from plunge-frozen *E. coli* cells by automated milling and subjected them to our acquisition and processing pipeline. In total, 3x multishot (Fig. 3A) tomograms were acquired on nine positions. Despite their average x-tilt of $\beta = \sim 5^{\circ}$, tracking and CTF were stable for all series (Supporting Fig. 5) and yielded 27 high quality tomograms, which were subjected to template matching and STA. From just 7.6k particles, an initial average with 14 Å resolution was obtained, proving that multishot tomography can indeed be used to quickly screen particles within intact cells. Higher resolution averages at 8.8 Å, where secondary structure elements are clearly visible (Fig. 3 C&D), were obtained using tilt-series refinement in STOPGAP_refine (Fig. 3B) or Warp/M[23] (Supporting Fig. 6).

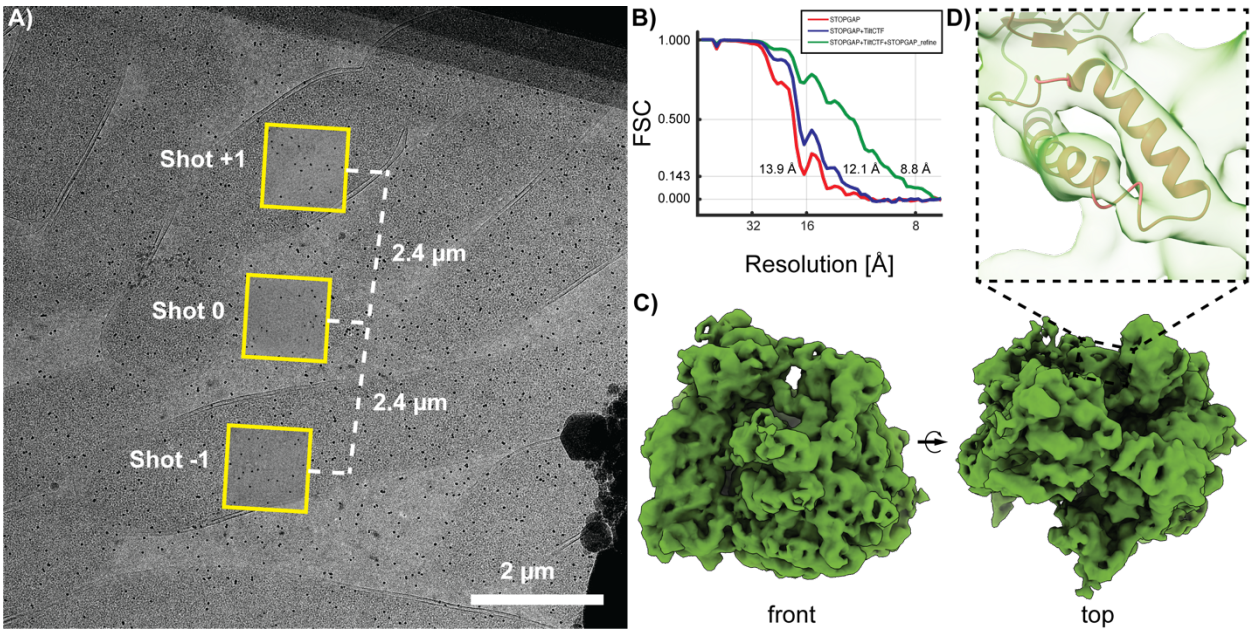

Figure 3. A) Setup of multishot tomograms on an automatically milled lamella of *E. coli*. B) Average and FSC plot from 7.6k in situ ribosome particles before computational refinement (27 tomograms from nine positions, each with 3x multishot series).

In Summary, we show that the obtainable resolution for subtomogram averaging is not affected when tilt series are acquired using beam image-shift axial multishot tomography. This method does not require external software and is straightforward to implement on cryo-EM microscopes, which are run using SerialEM. We show that this simple extension to the cryo-ET acquisition routine enables a faster, yet reliable way to collect tilt series without compromising data quality over throughput. Our method is applicable to both *in vitro* samples and in situ cryo-FIB milled lamellas, yielding high quality sub-nanometer subtomogram averages for biological investigations.

Methods

Sample Preparation

a) In Vitro Samples: For the mixed ribsome and proteasome dataset (subsequently called 'RiboProt'), purified *E. coli* 70S ribosomes and *T. acidophilum* 20S proteasomes at equimolar concentration (3.0 mg/mL and 1.5 mg/mL, respectively) were mixed with 10 nm gold fiducials (Aurion). 4.5 µl of this mixture were applied onto a glow-discharged 200 mesh Quantifoil R2/1 copper grid. For the T20S dataset, the purified *T. acidophilum* 20S proteasome sample was mixed with 10 nm gold fiducials, and 4.5 µl of the mix was applied onto a glow-discharged 200 mesh Quantifoil MultiA copper grid. The same procedure was used for purified RuBisCo complexes (C. reinhardtii) at 1.8 mg/mL For the carbon tilt-series dataset, a 1:4 suspension of 3x concentrated 10 nm gold fiducials (Aurion) in water was applied onto a glow-discharged 200 mesh Quantifoil MultiA copper grid.

In all cases, samples were vitrified in a liquid ethane/propane mixture using a Vitrobot Mark IV (Thermo Fisher Scientific) set to 4 ºC and 100% humidity. Settings: blot force = 20 or 8; blot time = 4.5 s; wait time = 0 s. Before loading, all grids were clipped in Autogrids (Thermo Fisher Scientific).

b) In Situ Samples: *E. coli* cells were grown in log phase conditions to an OD_{600} of 0.8. 4 µL of the cells were applied to a glow-discharged 200 mesh Quantifoil R2/1 copper grid and vitrified in a liquid ethane/propane mixture on a Vitrobot Mark IV (Thermo Scientific) set at 4 ºC and 100% humidity with backside blotting only. Settings: blot force = 10; blot time = 10 s; wait time = 1 s. Samples were stored under liquid nitrogen until use. Grids were clipped in modified Autogrids with a round cutout and subjected to automated FIB-milling on an Aquilos (Thermo Fisher Scientific) using AutoTEM cryo (Thermo Fisher Scientific) as described elsewhere.[24] After final milling, the samples were sputter coated with a thin layer of metallic platinum using the in-chamber plasma coater.

Data acquisition

The RiboProt and *E. coli* lamella datasets were collected using a Thermo Scientific Titan Krios equipped with Gatan Bioquantum energy filter and K2 summit Direct Electron Detector. Tilt-series were collected with a dose-symmetric tilt scheme[11] using SerialEM 3.8 with automated stigmation, coma-free alignment, and coma vs. image shift compensation.[3]

For the RiboProt datasets, the tilt range was ± 60º with 3º increments. In case of the RiboProt singleshot dataset, each tilt image was preceded by tracking and autofocus and was tracked after acquisition. In case of RiboProt multishot dataset, two shots in a hole without center shot were acquired at each tilt using the Multiple records dialogue (see protocol for detailed description). Each multiple records acquisition was preceded by a by tracking and autofocus. The second shot was tracked after each tilt. In both cases, target focus was changed per multishot tilt-series in steps of 0.25 µm over a range of -1.25 µm to -2.75 µm. Tilt

images were acquired in counting mode with a calibrated pixel size of 1.1 Å and total dose of 3 $e^-/Å^2$ over ten frames.

For the *E. coli* lamella dataset, tilt range was +49º to -66º with 3º steps starting at -10º to compensate for the pre-tilt. At each angle, two shots (±1) followed by a center shot (0) were acquired using the multiple records dialogue box. Each multiple records acquisition was preceded by tracking and autofocus. The center shot was tracked after each tilt. Target focus was changed per tilt-series in steps of 0.25 µm over a range of -1.25 µm to -2.75 µm. Tilt images were acquired in counting mode with a calibrated physical pixel size of 1.79 Å and total dose of 3 $e^-/Å^2$ over ten frames.

The *T. acidophilum* 20S proteasome, and carbon tilt-series datasets were collected using a Thermo Scientific Titan Krios G3i equipped with a modified Selectris X energy filter and Falcon4 direct detector. Tilt-series were collected with dose-symmetric tilt scheme[11] using SerialEM software.[3] Tilt range was ± 60º with 3º angular increments. At each tilt, five shots (±2, ±1, 0) were acquired using Multiple records dialogue box. Each multiple records acquisition was preceded by tracking and autofocus. The center shot was tracked before acquiring remaining four shots using a custom pattern. Target focus was changed per tilt-series in steps of 0.1 µm over a range of -0.8 µm to -2.2 µm. Tilt images were acquired in EER (Electron Event Registration) mode[25] with a calibrated physical pixel size of 1.224 Å and total dose of 3 $e^-/Å^2$.

Image processing

a) Tilt-series preprocessing and tomogram reconstruction: The data was preprocessed using TOMOgram MANager (TOMOMAN) [26]. In case of K2 summit data acquisition, MOTIONCOR2[27] was used for motion correction. For Falcon 4 EER data, motion correction was performed using Relion's implementation of MOTIONCOR with EER support[28]. The tilt-series were corrected for dose-exposure using MATLAB (MathWorks) scripts adapted for tilt series[26]. Defocus was estimated using CTFFIND4[29]. Tilt series were aligned using fiducial based alignment in IMOD[30]. In case of RiboProt, T20S proteosome, and carbon tilt-series datasets, gold beads were automatically selected and tracked. In case of the in situ *E. coli* dataset, ~ 25 nm platinum granules (resulting from the Pt-sputter coating) were automatically selected and tracked. The resulting fiducial model was corrected manually in all cases where automatic selection and tracking failed. Tilt series alignment was computed without solving for any distortions. Initial tomograms without CTF correction were reconstructed by weighted back projection (WBP) at 8x binning and used for template matching[22]. For subtomogram averaging, tomograms were reconstructed with 3D-CTF correction using novaCTF [31] with phase-flip correction, astigmatism correction using 15 nm slab thickness. Tomograms were binned 2x, 4x, and 8x using FourierCrop3D[31].

b) Subtomogram Averaging

Initial particle positions and orientations were determined using noise correlation template matching approach implemented in STOPGAP[22]. Subsequent subtomogram averaging and classification were performed using STOPGAP[22]. Classification was performed using simulated annealing stochastic hill climbing multi reference alignment as described before[32].

c) Tilt-Series Refinement

In case of the 70S Ribosome from cryo-FIB milled E.coli lamellas, we performed tilt series refinement using STOPGAP_refine[15] as well as Warp/M/Relion3.0 pipeline[14]. In both cases, the tilt -series refinement was performed on 2x binned data and resulted in 8.8 Å 70S ribosome average.

d) Data visualization and statistics

Wherever applicable, data statistics was calculated and plotted using custom scripts written MATLAB (Mathworks). Subtomogram averages were visualized using ChimeraX[33]. Atomic models were docked into the electron density maps using rigid body docking in ChimeraX[33]. The model to map fit was refined using ISOLDE[34].

Data/Material Availability

The raw cryo-ET datasets that support the findings of this study have been uploaded to EMPIAR and can be downloaded using accession codes ~~XXX~~, ~~YYY~~, and ~~ZZZ~~. Cryo-EM maps have been deposited on EMDB and can be accessed using codes ~~XXX~~. [These will be available upon publication or by reviewer request]

Literature

1. Kühlbrandt, W. The resolution revolution. *Science (80-.).* **343**, 1443–1444 (2014).
2. Mcmullan, G., Faruqi, A. R. & Henderson, R. Direct Electron Detectors. *Resolut. Revolut. Recent Adv. cryoEM* **579**, 1–17 (2016).
3. Mastronarde, D. N. Advanced Data Acquisition From Electron Microscopes With SerialEM. *Microsc. Microanal.* **24**, 864–865 (2018).
4. Carragher, B. *et al.* Leginon: {An} {Automated} {System} for {Acquisition} of {Images} from {Vitreous} {Ice} {Specimens}. *J. Struct. Biol.* **132**, 33–45 (2000).
5. Scheres, S. H. W. {RELION}: {Implementation} of a {Bayesian} approach to cryo-{EM} structure determination. *J. Struct. Biol.* **180**, 519–530 (2012).
6. Grant, T., Rohou, A. & Grigorieff, N. CisTEM, user-friendly software for single-particle image processing. *Elife* **7**, (2018).
7. Tegunov, D., Xue, L., Dienemann, C., Cramer, P. & Mahamid, J. Multi-particle cryo-EM refinement with M visualizes ribosome-antibiotic complex at 3.5 Å in cells. *Nat. Methods 2021 182* **18**, 186–193 (2021).
8. Wang, Z. *et al.* Structures from intact myofibrils reveal mechanism of thin filament regulation through nebulin. *Science* **375**, eabn1934 (2022).
9. von Kügelgen, A. *et al.* In Situ Structure of an Intact Lipopolysaccharide-Bound Bacterial Surface Layer. *Cell* **180**, 348-358.e15 (2020).
10. Chreifi, G., Chen, S., Metskas, L. A., Kaplan, M. & Jensen, G. J. Rapid tilt-series acquisition for electron cryotomography. *J. Struct. Biol.* **205**, 163–169 (2019).
11. Hagen, W. J. H., Wan, W. & Briggs, J. A. G. Implementation of a cryo-electron tomography tilt-scheme optimized for high resolution subtomogram averaging. *J. Struct. Biol.* **197**, 191–198 (2017).
12. Eisenstein, F., Danev, R. & Pilhofer, M. Improved applicability and robustness of fast cryo-electron tomography data acquisition. *J. Struct. Biol.* (2019) doi:10.1016/j.jsb.2019.08.006.
13. Himes, B. A. & Zhang, P. emClarity: software for high-resolution cryo-electron tomography and subtomogram averaging. *Nat. Methods* **15**, 955–961 (2018).
14. Tegunov, D., Xue, L., Dienemann, C., Cramer, P. & Mahamid, J. Multi-particle cryo-EM refinement with M visualizes ribosome-antibiotic complex at 3.5 Å in cells. *Nat. Methods* **18**, 186–193 (2021).
15. Khavnekar, S., Wan, W., Erdmann, P. & Plitzko, J. STOPGAP_refine: Tilt series refinement for high-resolution subtomogram averaging. *Microsc. Microanal.* **27**, 3240–3240 (2021).
16. Cheng, A. *et al.* High resolution single particle cryo-electron microscopy using beam-image shift.

J. Struct. Biol. **204**, 270–275 (2018).

17. Mastronarde, D. N. Automated electron microscope tomography using robust prediction of specimen movements. *J. Struct. Biol.* **152**, 36–51 (2005).
18. Bouvette, J. *et al.* Beam image-shift accelerated data acquisition for near-atomic resolution single-particle cryo-electron tomography. *Nat. Commun. 2021 121* **12**, 1–11 (2021).
19. Turoňová, B. *et al.* Benchmarking tomographic acquisition schemes for high-resolution structural biology. *Nat. Commun.* **11**, 1–9 (2020).
20. Bouvette, J. *et al.* Beam image-shift accelerated data acquisition for near-atomic resolution single-particle cryo-electron tomography. *bioRxiv* 2020.09.24.294983 (2020) doi:10.1101/2020.09.24.294983.
21. Bharat, T. A. M. & Scheres, S. H. W. Resolving macromolecular structures from electron cryo-Tomography data using subtomogram averaging in RELION. *Nat. Protoc.* **11**, 2054–2065 (2016).
22. Wan, W. williamnwan/STOPGAP: STOPGAP 0.7.1. (2020) doi:10.5281/ZENODO.3973664.
23. Tegunov, D., Xue, L., Dienemann, C., Cramer, P. & Mahamid, J. Multi-particle cryo-EM refinement with M visualizes ribosome-antibiotic complex at 3.7 Å inside cells. *bioRxiv* 2020.06.05.136341 (2020) doi:10.1101/2020.06.05.136341.
24. Tacke, S. *et al.* A streamlined workflow for automated cryo focused ion beam milling. *bioRxiv* 2020.02.24.963033 (2020) doi:10.1101/2020.02.24.963033.
25. Guo, H. *et al.* Electron-event representation data enable efficient cryoEM file storage with full preservation of spatial and temporal resolution. *urn:issn:2052-2525* **7**, 860–869 (2020).
26. Wan, W. williamnwan/TOMOMAN: TOMOMAN 08042020. (2020) doi:10.5281/ZENODO.4110737.
27. Zheng, S. Q. *et al.* MotionCor2: anisotropic correction of beam-induced motion for improved cryo-electron microscopy. *Nat. Methods 2017 144* **14**, 331–332 (2017).
28. Nakane, T. *et al.* Single-particle cryo-EM at atomic resolution. *Nat. 2020 5877832* **587**, 152–156 (2020).
29. Rohou, A. & Grigorieff, N. CTFFIND4: Fast and accurate defocus estimation from electron micrographs. *J. Struct. Biol.* **192**, 216–221 (2015).
30. Mastronarde, D. N. & Held, S. R. Automated tilt series alignment and tomographic reconstruction in {IMOD}. *J. Struct. Biol.* **197**, 102–113 (2017).
31. Turoňová, B., Schur, F. K. M., Wan, W. & Briggs, J. A. G. Efficient 3D-CTF correction for cryo-electron tomography using NovaCTF improves subtomogram averaging resolution to 3.4 Å. *J. Struct. Biol.* **199**, 187–195 (2017).
32. Erdmann, P. S. *et al.* In situ cryo-electron tomography reveals gradient organization of ribosome

biogenesis in intact nucleoli. *Nat. Commun. 2021 121* **12**, 1–9 (2021).

33. Pettersen, E. F. *et al.* UCSF ChimeraX: Structure visualization for researchers, educators, and developers. *Protein Sci.* **30**, 70–82 (2021).

34. Croll, T. I. ISOLDE: A physically realistic environment for model building into low-resolution electron-density maps. *Acta Crystallogr. Sect. D Struct. Biol.* **74**, 519–530 (2018).

Author Contributions

PSE, SK and JMP designed the study. SK, W. Wi and PM prepared materials. SK and PSE collected data. SK, PSE and W.Wa wrote software and processed the data. SK, PSE and JMP wrote the manuscript with suggestions and comments from all authors.

Supporting Material

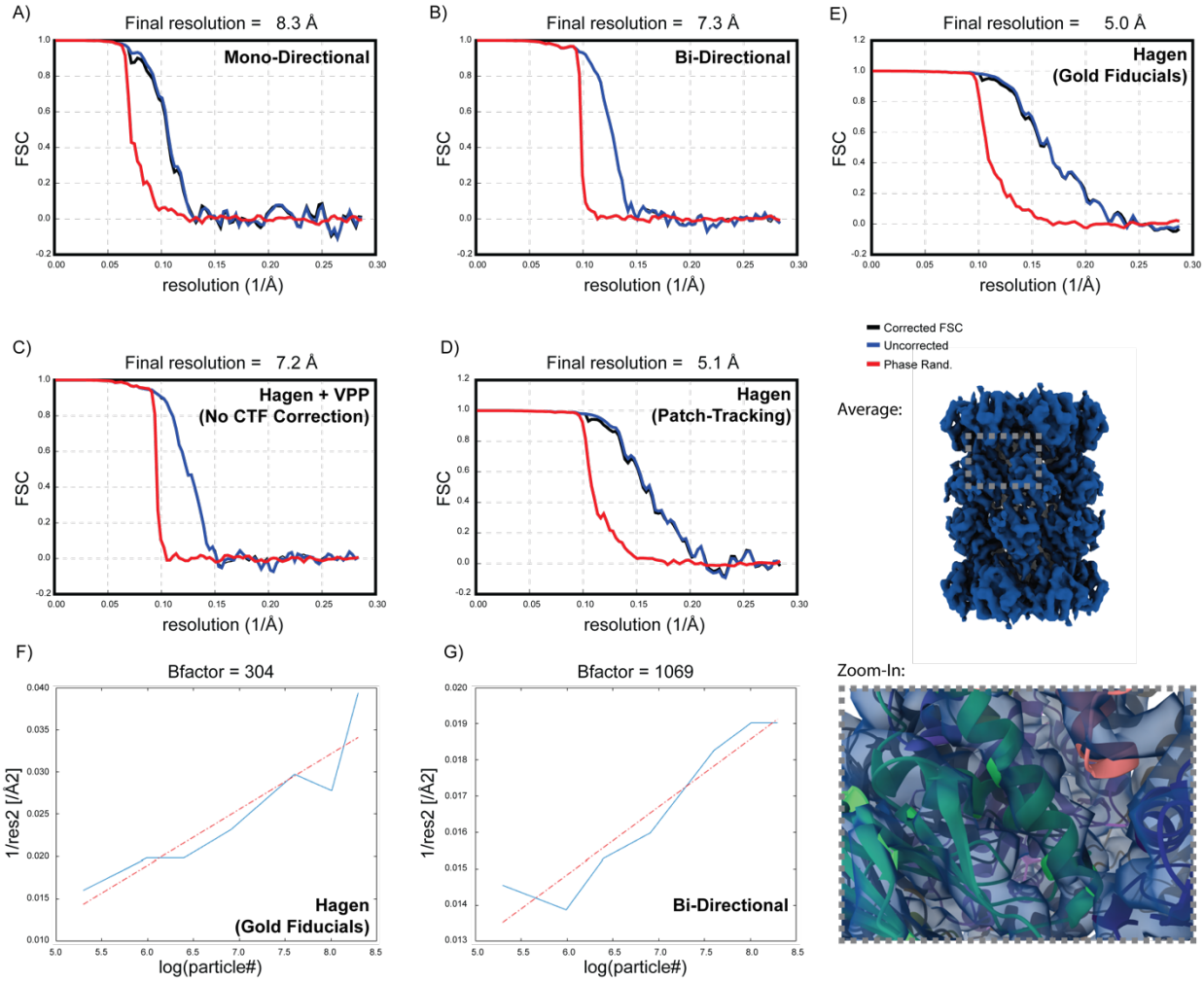

Supporting Figure 1. Evaluating the performance of different tilting and acquisition schemes on a *T. acidophilum* 20S proteasome sample: monodirectional (A), bi-directional (B), dose-symmetrical with the Volta Phase Plate (VPP; C), dose-symmetrical using defocus imaging and patch tracking (D), and dose-symmetrical using gold fiducials (E). (FSC = 0.143 criterion). F) and G) Corresponding log-res plots for schemes E and B, respectively. Insert shows STA average of the Hagen (Patch Tracking) results with a zoom-in on a secondary structure element.

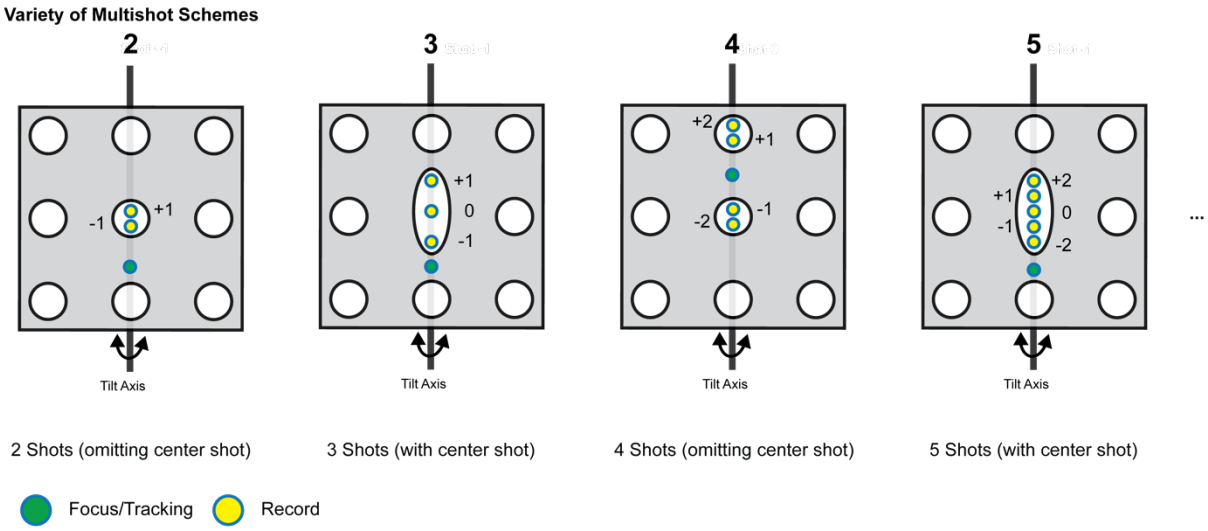

Supporting Figure 2. Schematic and numbering of different multishot series from two to five shots on regular grids using built-in SerialEM functions. For perfectly aligned samples with regular geometry, shots can be acquired across holes. For special types like MultiA (elongated holes, e.g. 3 & 5), multiple areas can be acquired within the same hole. However, their arrangement can be disregarded for other sample types such as lacey grids or FIB lamellas.

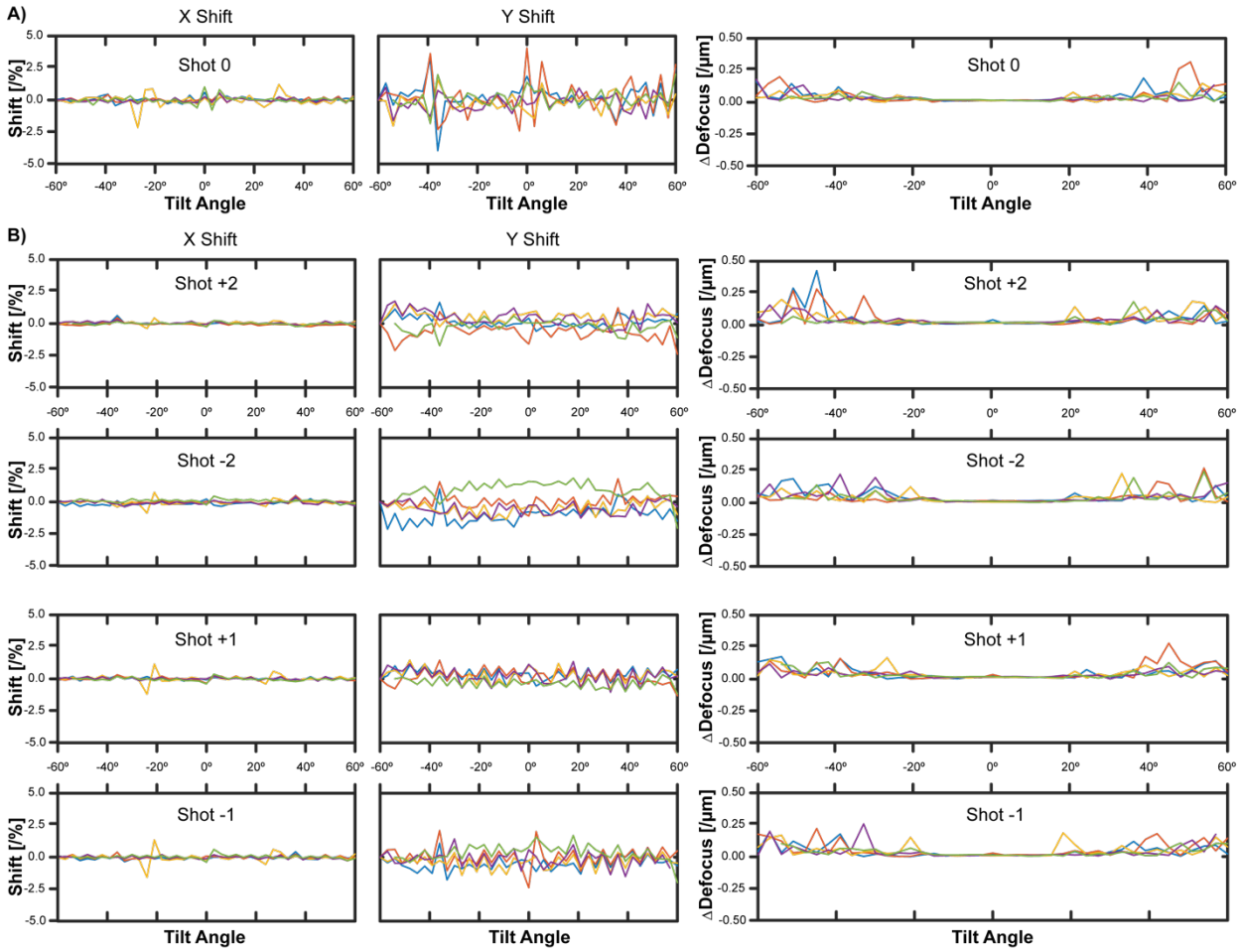

Supporting Figure 3. Carbon 5x axial multishot series. A) Alignment data for the zero shot (0) of a five-shot series. B) Alignment data for the remaining four shots (±1, ±2).

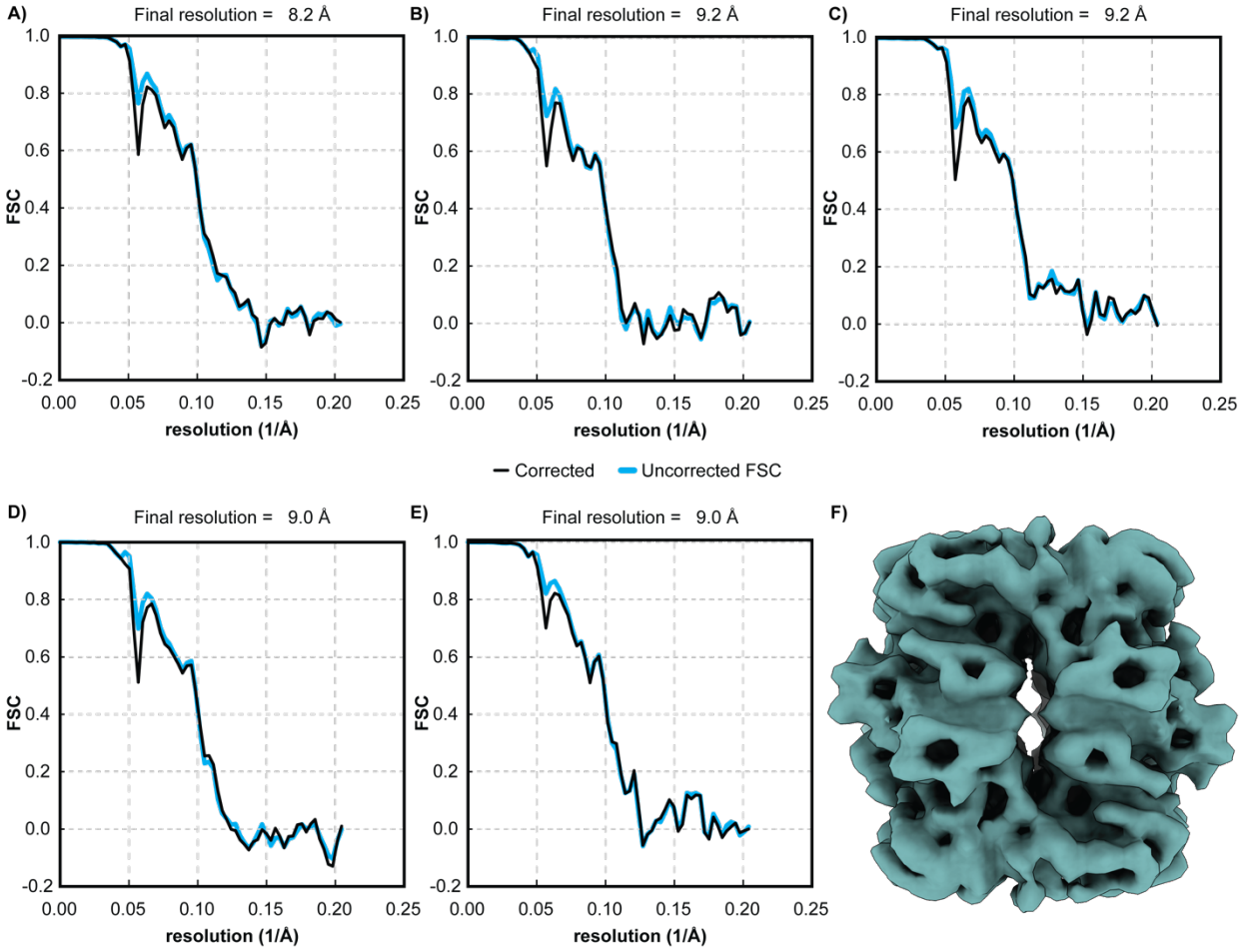

Supporting Figure 4. STA results for a 5x axial multishot series on RuBisCo. In the order of acquisition 0, +1, –1, +2, -2 (A-E). F) Consensus map after reconstruction and sharpening (Relion).

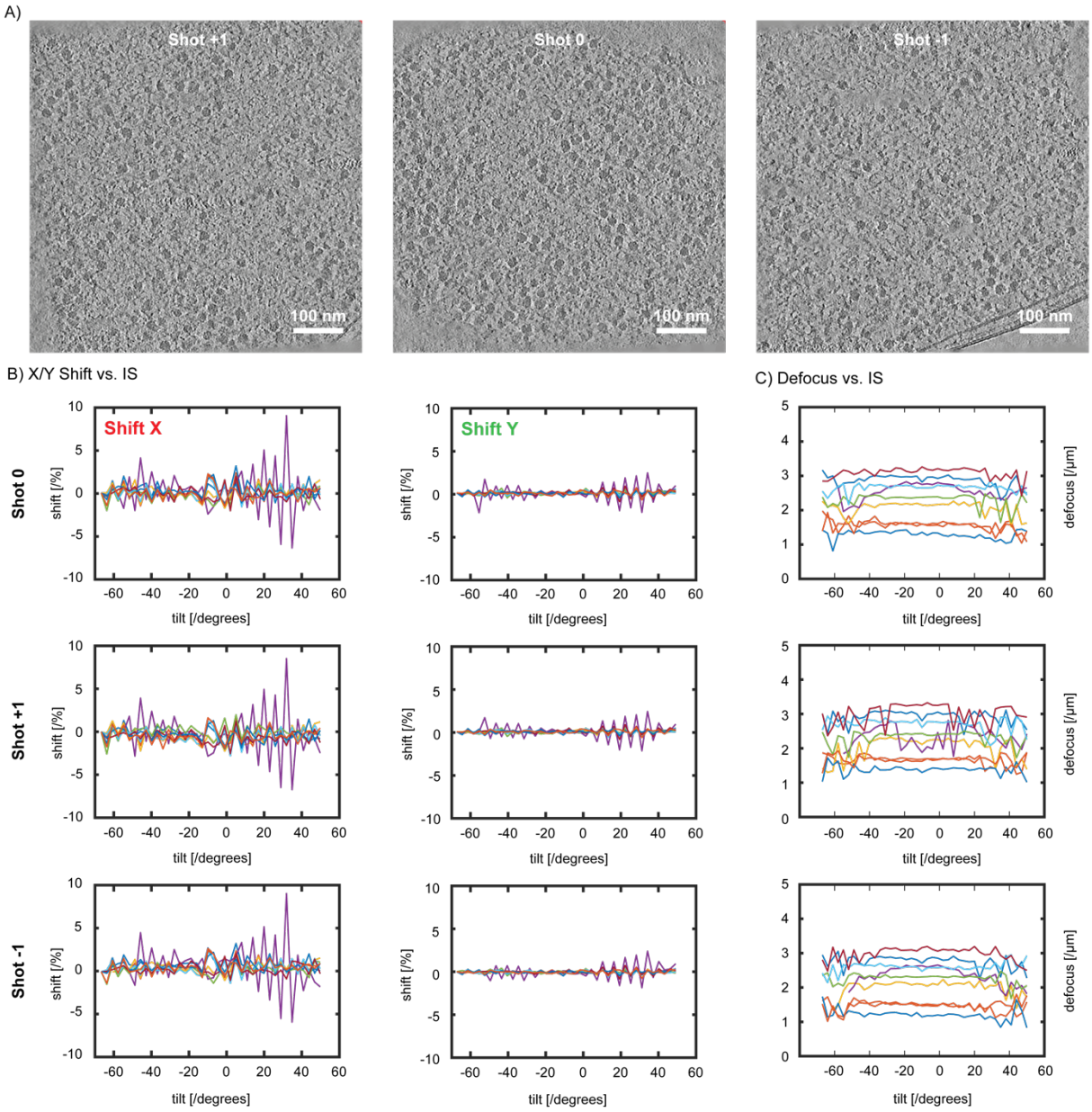

Supporting Figure 5. A) Representative slices through the middle of the tomograms of a three-shot in situ series on E. coli lamellas. B) Alignment and C) Defocus vs. image shift for the three-shot series consisting out of 27 tomograms (3x9) in total.

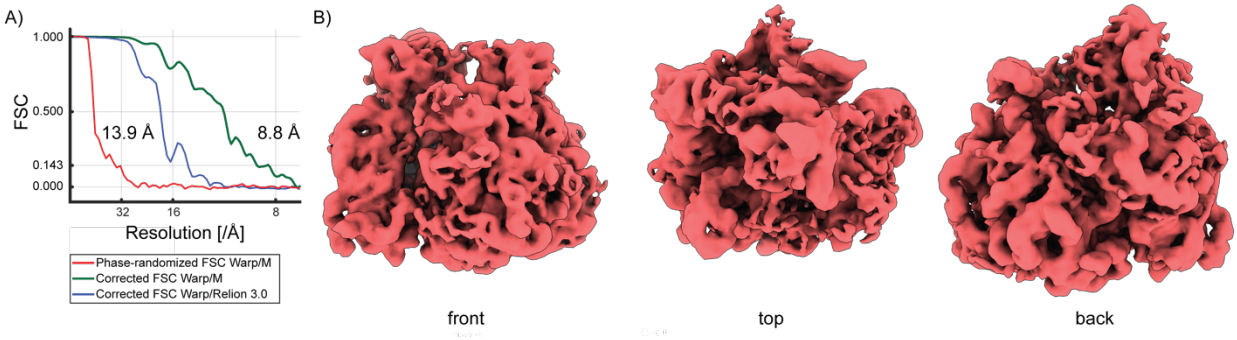

354

355 **Supporting Figure 6.** A) Resolution before and after refinement in Warp/M (FSC = 0.143 cutoff), and B) ribosome STA
356 maps after refinement.